Influence of air-entraining agent and freeze-thaw action on pore structure in high-strength concrete by using CT-Scan technology

Dorys C. González[1,*], Álvaro Mena[1], Jesús Mínguez[1] and Miguel A. Vicente[1]

[1] University of Burgos, Dpt. Civil Engineering, C/ Villadiego s/n, 09001 Burgos, Spain.

* Correspondence: dgonzalez@ubu.es; Tel.: +34-947-25.94.20

Abstract

In this work, the effects caused by both the amount of air-entraining agent (AEA) and freeze-thaw cycles on microstructure of high-strength concrete have been analyzed. For this purpose, five series of concrete specimens have been manufactured, each of them containing a different amount of AEA. Then, all series have been subjected to up to 300 freeze-thaw cycles. In addition, the specimens have been analyzed-using a computed tomography (CT) scan device at pre-defined freeze-thaw cycles and all data have been processed with digital image processing (DIP) software.

The results reveal, on the one hand, that the quantity of AEA has a greater influence on pore structure, and additionally the freeze-thaw action only slightly modifies the pore structure. As AEA increases, a progressive rise of the porosity and the number of pores is observed up to a maximum value. Next, a decrease is noticed. Moreover, there is not a linear relation between porosity and AEA. Furthermore, as AEA increases, a variation of its size and shape is observed. Alternatively, the effect of freeze-thaw cycles is more complex and does not show a monotonous tendency. The results reveal that the first 50 freeze-thaw cycles have the strongest influence on pore structure, observing a decrease in porosity. For the rest of the cycles, the porosity increases progressively resulting, after 300 freeze-thaw cycles, in a slightly lower porosity in almost all series than in those presented at the beginning. Hydration of unhydrated cement particles alongside with microcracking act as opposite performances during the freeze-thaw cycles. Therefore, this can suggest that, under these conditions, freeze-thaw action is not able to damage significantly the microstructure of concrete.

The results show that the series with a lower AEA content show a better behavior under freeze-thaw cycles. In this case, the specimens exhibit a lower porosity and a higher level of small pores, and the pores evince a more elongated shape. All these features lead to a more impermeable concrete and, therefore, with a better performance under freeze-thaw cycles.

Keywords: computed tomography; air-entraining agent; freeze-thaw cycles; high-strength concrete; pore structure; pore distribution.

1. Introduction

Freeze-thaw action has a determining influence on service life of concrete structures located in many cold regions of the planet. As temperature decreases below 0°C, the free water into concrete freezes and increases in volume, bringing along with it an increase in pressure. When temperature rises above 0°C, the free water returns to its original liquid form, leading to a decrease on the internal pressure. The repeated action of this freeze-thaw process cause, in concrete structures, the birth and growth of microcracks. This phenomenon, along with the action of external loads, can result in structural collapse (Kosior-Kazberuk, 2013; Ma et al., 2017; Shields et al., 2018). This nature of cumulative damage is the reason why this mechanism is also known as thermal fatigue.

Pores have a key role in the strength of concrete structures against freeze-thaw cycles; particularly in the water unsaturated ones. Their most direct influence lies in the fact that they act as a reserve of volume against water expansion when freezing. In this way, the unsaturated pores are able to reduce the internal pressure of concrete. Thus, it is common for structural standards in cold regions to require the use of AEA in concrete manufacturing with the aim of assuring a suitable freeze-thaw strength (ASTM C226-19, 2019; UNE-EN 206, 2018).

The role of AEA is to introduce air into the concrete matrix shaped like stable microbubbles, whose size is about one tenth of a millimeter (100 μm) (Jianxun et al., 2014). As a result, high porosity is achieved. However, porosity (defined as the ratio between the volume of trapped air and the total volume of concrete) is a global parameter that does not completely define the behavior of concrete under freeze-thaw cycles. In this sense, there is some recent research that highlights the key role of concrete microstructure (Dong et al., 2018; Han and Tian, 2018; Luo et al., 2017; Netinger Grubeša et al., 2019; Shields et al., 2018; Suzuki et al., 2017; Tian and Han, 2018). Therefore, it is interesting to study not only porosity, but also all the parameters related to pore structure (size, shape, distribution, etc.).

Pores also affect the response of concrete against mechanical stresses. A number of semi-empirical relationships between porosity and concrete strength can be found in scientific literature. The most remarkable ones are those belonging to Balshin (1949), Ryshkewitch (1953), Schiller (1958) and Hasselman (1963). In all of them, it is stablished that an increase in porosity involves a loss of compressive, tensile and flexural strength. In the case of mechanical fatigue, although its study is much more recent, a decrease in fatigue life while porosity increases has been observed (Chen et al., 2013; Vicente et al., 2018a).

The interaction between freeze-thaw cycles and mechanical response of concrete structures is of great interest. This phenomenon is observed in concrete bridges and concrete wind turbine towers located in regions subjected to thermal fatigue cycles, as in the north of USA and south of Canada, the north of Europe or China and south of Russia, among others. In addition to thermal fatigue, these structures are subjected to external loads of both static and dynamic nature, as well as to mechanical fatigue. In both cases, high-strength concrete is commonly used.

As with thermal fatigue, mechanical fatigue results in a progressive degradation of the internal microstructure of concrete (Fan and Sun, 2019; Skarżyński et al., 2019; Vicente et al., 2018b, 2018a). In consequence, it is expected to find an addition of both the effects caused by the different types of fatigue, resulting in the acceleration of the birth and growth of the microcracking, and a reduction of the service life of the structure. However, few works thereon have been published so far, most of these focused on the study of concrete pavements (Shen et al., 2018; Yang et al., 2018).

According to IUPAC, pores can be classified according to their size into micropores (smaller than 2 nm), mesopores (from 2 to 50 nm) and macropores (larger than 50 nm) (Le et al., 2015; Rouquerol et al., 1994; Vydra et al., 2001). The traditional methods to analyze the pore structure are nitrogen absorption and mercury-intrusion porosimetry (MIP) (Gu et al., 2018; Netinger Grubeša et al., 2019), even though they have important limitations. On the one hand, they can only provide the pore-size distribution, but neither their spatial distribution nor their morphological parameters can be demonstrated. On the other hand, the information that they provide is related to the open porosity and not to the close one, which is rather more interesting when studying this phenomenon.

Nowadays, the use of computed tomography (CT) scanning technology in the analysis of concrete microstructure is increasingly common. In this field, there are many research works mainly focused on fiber-reinforced concrete, in which several parameters concerning fiber distribution and orientation are analyzed (Gao et al., 2018; González et al., 2018; Jasiūnienė et al., 2018; Oesch et al., 2018; Skarżyński and Suchorzewski, 2018; Miguel A. Vicente et al., 2019b). Additionally, in recent years computed tomography (CT) has begun to be applied for the study of concrete pore morphology (Mínguez et al., 2019; Nitka and Tejchman, 2018; Olawuyi and Boshoff, 2017; Zhao et al., 2019; Zhou et al., 2019).

CT-Scan technology is able to isolate all pores of any concrete specimen with a minimum size of about 10 μm; namely, macropores. Moreover, much information can be obtained about every single element: position, volume, surface, length, etc. This way, statistical studies can be carried out with these parameters or even with some previous obtained data, such as the shape factor, etc.

The aim of this work is to study the changes produced in the pore structure of high-strength concrete due to two variables: the amount of AEA and the freeze-thaw action. For that purpose, concrete specimens with different amounts of AEA have been casted, and then they have been subjected up to 300 freeze-thaw cycles. Additionally, the specimens have been scanned by using a CT-scan at pre-defined number of cycles (0, 50, 100 and 300 cycles). The results obtained enable to define several correlations between the variables under study and the evolution of concrete microstructure. High-strength concrete is commonly used in concrete bridges and concrete wind turbine towers.

The innovation of this paper is the use of computerized tomography to study the variation of the porosity of concrete subjected to freeze-thaw cycles. The computerized tomography allows the evaluation of many parameters of the pores (much more than other methods commonly used for the measurement of porosity), such as pore-size distribution, pore length and shape factor. These parameters can be therefore correlated to the behavior of the specimen under freeze-thaw cycles, in order to investigate the impact of the microstructure on their macroscopic response.

This paper is structured as follows. The experimental procedure is presented in Section 2; the results obtained are described and discussed in Section 3; the correlation between internal microstructure and behavior under freeze-thaw cycles is described in Section 4; and finally, the conclusions are found in Section 5.

2. Experimental program

2.1. Materials

In this research, 60 specimens divided in 5 series have been casted, which results in 12 specimens per individual series. The only difference between each series is the amount of AEA, which has been gradually increased from series A0.0 (0%) to series A0.4 (0.4%). The percentages of AEA have been chosen considering that 0.3% is the maximum amount recommended by the AEA manufacturer. Table 1 shows the dosage of concrete used in each series. As can be observed, some series show a quantity of AEA lower than the maximum recommended, while series A0.4 shows an amount greater than the maximum recommended.

Portland cement with high initial strength CEM I 52.5 R was used together with siliceous fine aggregate with a maximum size of 4 mm and coarse aggregate with a size between 4 and 6 mm. The AEA used was MasterAir 100 (BASF, Ludwigshafen am Rhein, Germany). Finally, superplasticizer MasterGlenium 51 (BASF, Ludwigshafen am Rhein, Germany) and nanosilica MasterRoc MS 685 (BASF, Ludwigshafen am Rhein, Germany) were used.

Table 1. Concrete mixture.

Dosage	A0.0	A0.1	A0.2	A0.3	A0.4
Cement (kg/m3)			700.0		
Water (kg/m3)			219.0		
Superplasticizer (kg/m3)			22.0		
Nanosilica (kg/m3)			10.0		
Fine Aggregate (kg/m3)			685.0		
Coarse Aggregate (kg/m3)			794.0		
Air Entraining Agent (kg/m3)	0.00	0.72	1.44	2.16	2.88
Ratio AEA/Cement	0.0%	0.1%	0.2%	0.3%	0.4%

The specimens tested are cubic with an edge of 40 mm, and they have been obtained from prismatic specimens with a size of 40x40x160 mm. A 2.8 mm-thickness diamond disc has been used for the cut. A total of 3 cubic specimens have been cut off from every prismatic specimen, so the ends of the prism have been discarded (Figure 1).

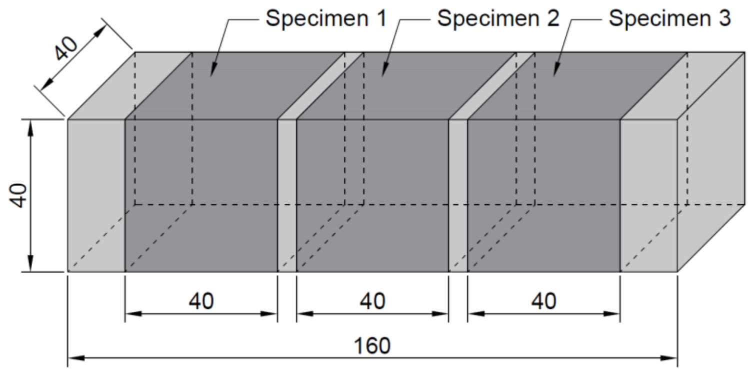

Figure 1. Cubic specimen extraction from prismatic specimen.

The specimens were cured for 90 days in a climatic chamber at a relative humidity of 97%±0.3% and an ambient temperature of 20 °C ± 0.5 °C. All the specimens were approximately 90 days-old at the start of the test campaign.

2.2. Testing procedure

Out of the 12 specimens of each series, 3 of them have been subjected to uniaxial compression test, following the European standard UNE-EN 12390-3 (2020), in order to determine the average compression strength of concrete (f_{cm}). Table 2 shows the results obtained, together with the standard deviation in brackets. Besides, 9 specimens of each series have been subjected up to 300 freeze-thaw cycles, according to ASTM C666/C666M-15 (2015) standard. The range of temperatures in every cycle is stablished between -18°C y 4°C, and the tolerance of the equipment used is ±1°C. A freezing chamber with temperature monitoring has been used during freezing, while a common cold store was used for thawing. Temperature has been systematically controlled at the beginning and the end of every stage. The total duration of every freeze-thaw cycle was 2 hours, with both stages being equal (1 hour). However, as mentioned in the American standard, during the time that it was not possible to continue with freeze-thaw cycles, the specimens were kept in frozen condition (-18°C) to avoid the loss of moisture.

Table 2. Average compression strength of concrete and standard deviation.

Series	f_{cm} (MPa)
A0.0	98.4 (1.5)
A0.1	99.8 (0.9)
A0.2	92.3 (3.2)
A0.3	88.6 (3.0)
A0.4	91.3 (2.7)

2.3. CT scanning and image postprocessing

Each specimen has been scanned four times: the first one before starting the freeze-thaw test and three times during its development; more specifically, at 50, 100 and 300 cycles. The CT-scan used is a GE Phoenix v|tome|x (General Electric, Boston, MA, USA) device. It is equipped with an X-ray tube of 300 kV/500 W. This facility includes a software that provides sectional images of the specimens with a resolution of 2048x2048 pixels. Both the pixel size and the spacing between consecutive slices is 35 μm, so the voxel size (volumetric pixel) is 35x35x35 μm^3. Thus, a total of 1334 images can be obtained from each specimen.

The software included in the CT-scan works with 8-bit images, so a grey value in a range varying from 0 to 255 is assigned to each voxel, where 0 means black and 255 means white. The value assigned depends on the linear attenuation coefficient μ of the material, which in turn depends on density. Therefore, light grey voxels (high values) belong to more dense points, while dark grey voxels (low values) belong to less dense points. For instance, pores are shown in black since they are filled with air, whose density is very low. Finally, as a result of the scanning process, a matrix including X, Y and Z coordinates of the center of gravity of each voxel as well as its grey value is obtained. The total number of voxels per specimen is approximately $1.7 \cdot 10^9$. The average scanning time of each specimen is about 1 hour. More detailed information regarding computed tomography can be found in (Miguel A Vicente et al., 2019; Vicente et al., 2017, 2014).

Next, image postprocessing has been carried out using the digital image processing (DIP) software AVIZO (FEI Visualization Sciences Group, Hillsboro, OR, USA). This tool enables identification and isolation of each individual pore into the specimens. First, the software identifies the voxels belonging to pores, which are the ones whose grey values are under the threshold value. With the aim of selecting a suitable threshold value, the histograms of grey distribution of all specimens have been studied. As a result, it is concluded that a grey value of 28 fits reasonably well into the pore-matrix interface. Figure 2 shows an example of a histogram of grey distribution, in which the threshold value of 28 is highlighted.

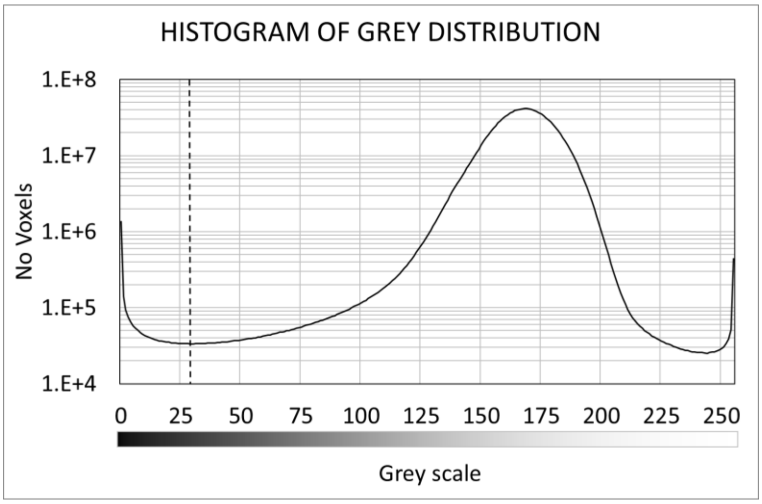

Figure 2. Example of a histogram of grey distribution. The threshold grey value (28) is highlighted in dotted line, so voxels with a grey value between 0 and 28 are considered as pores.

As illustrated in Figure 2, a grey value of 28 corresponds to the minimum of the histogram function. This means that this grey value corresponds to the border between the holes (darker voxels and more habitual) and the concrete matrix (whiter voxels, and also more common). Considering all voxels with a grey value below 28, it is guaranteed that the entire volume of each pore is captured.

After that, the DIP software merges the voxels in contact, creating groups that correspond to the pores into the concrete specimens. Figure 3 shows the pores identified and isolated in one specimen of each series. Finally, many data of every individual pore can be obtained: X, Y and Z coordinates of the center of gravity, as well as its volume, surface, length, etc. The length of a pore is defined as the maximum distance between two voxels belonging to the same pore. In this work, only pores equal to or greater than 0.1 mm have been considered; that is, with more than 3 voxels in their largest direction. The remaining ones have been discarded since their parameters cannot be determined with sufficient accuracy. The results shown are the average values of the 9 specimens of each series. In all cases, the variability between samples belonging to the same series was very low.

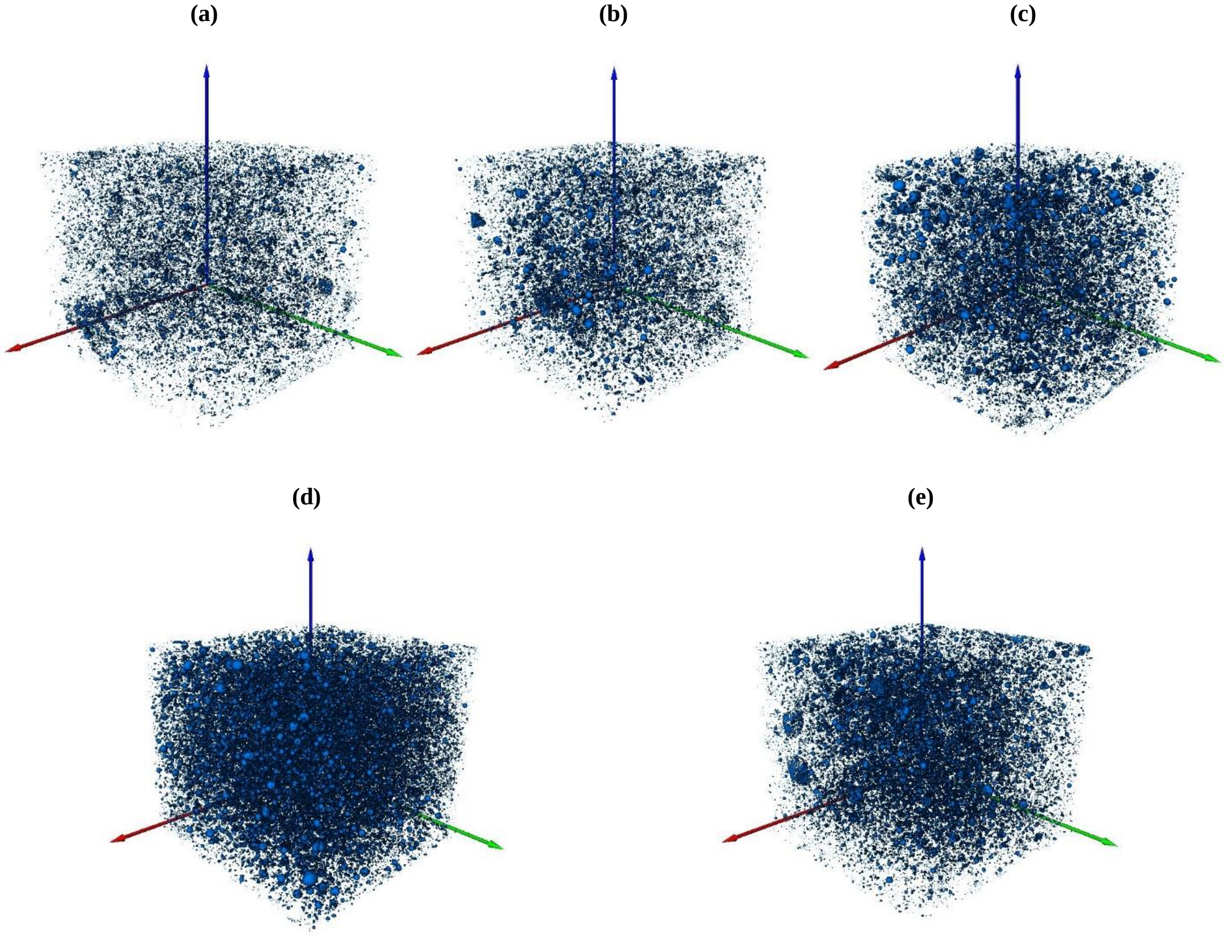

Figure 3. 3D reconstructed images of pore distribution in specimens of series A0.0 (a), A0.1 (b), A0.2 (c), A0.3 (d) and A0.4 (e). They were obtained after 100 freeze-thaw cycles.

3. Results and discussion

As a result of the CT scanning and the subsequent postprocessing through the DIP software, a large amount of information about every individual pore is obtained. In order to study the pore structure depending on the amount of AEA and the freeze-thaw action, an in-depth analysis has been carried out, focused on the most interesting parameters. In this case, a global study of pore-size distribution has been developed first, and then several particular analyses about two significant parameters – length and shape factor – have been carried out.

3.1. Pore-size distribution

Two different types of curves are commonly used to analyze the pore-size distribution. Firstly, the porosity curves relate the size of each pore with the porosity that the smaller pores represent. Therefore, porosity is displayed in the ordinate axis, defined as the ratio between the volume of pores considered (V_p) and the volume of the specimen (V_s) (Eq. (1)).

$$p = \frac{V_p}{V_s} \tag{1}$$

Secondly, the cumulative pore-volume curves relate the size of each pore with the relative volume of the smaller pores. Thus, relative pore-volume is displayed in the ordinate axis, defined as the ratio between the volume of pores considered (V_p) and the total volume of pores of the specimen ($V_{p,tot}$) ((Eq. (2)).

$$V_{p,rel} = \frac{V_p}{V_{p,tot}} \tag{2}$$

Figures 4 and 5 show the porosity curves and the cumulative pore-volume curves, respectively. All series have been plotted in both graphs, also considering the effect of freeze-thaw cycles. The values shown in Figures 4 and 5 correspond to the average values of each series.

In Figure 4, it is clearly observed that the amount of AEA has a decisive influence on concrete microstructure in general and on porosity in particular. When only the 0-cycle curves are compared, it is noticed that series A0.0, which does not contain any AEA, has the lower porosity. The addition of AEA causes an increase in porosity, as expected, until the maximum dosage recommended by the manufacturer is reached, which in this case corresponds with series A0.3. From then on, a decrease in porosity is observed (Table 3). These results match with those belonging to other investigations in which the influence of AEA on concrete porosity is also analyzed (Kim et al., 2012; Vicente et al., 2018a).

Table 3. Initial porosity (0 freeze-thaw cycles).

Series	Porosity (%)	Pore density (mm^{-3})	Maximum pore size, D_{90} (mm)
A0.0	0.43	0.73	1.32
A0.1	0.45	0.73	1.49
A0.2	1.49	1.13	2.62
A0.3	1.78	1.24	2.42
A0.4	1.11	0.99	1.85

With the aim of understanding the causes that explain the increase in porosity with the amount of AEA, the results in Table 3 and Figure 5 can be referred. Firstly, Table 3 reveals that pore density (defined as the number of pores per mm^3) increases with AEA, which means that the number of pores also does. Secondly, the maximum pore size (D_{90}) can be obtained from the cumulative pore-volume curves (Figure 5), defined as the size that is only exceeded by 10% of the total pores. It is a parameter often used to characterize the pore-size distribution of a specimen. The maximum pore size of each series at 0 freeze-thaw cycles is presented in Table 3. An increase in its value is observed with the amount of AEA, which implies that the pore size also increases. This fact is also observed in Figure 5 through a displacement of the cumulative pore-volume curves to the right.

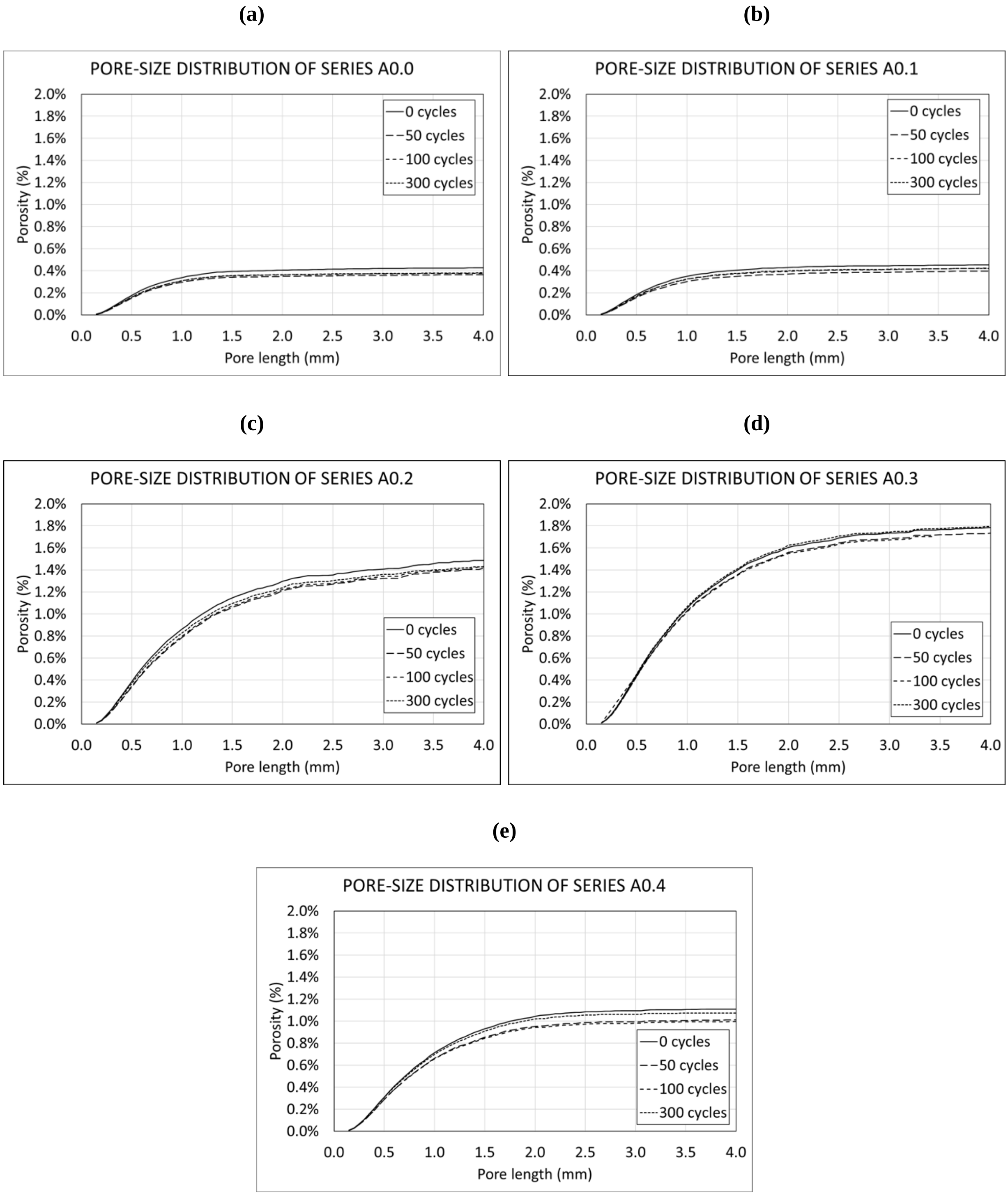

Figure 4. Porosity curves of series A0.0 (a), A0.1 (b), A0.2 (c), A0.3 (d) and A0.4 (e).

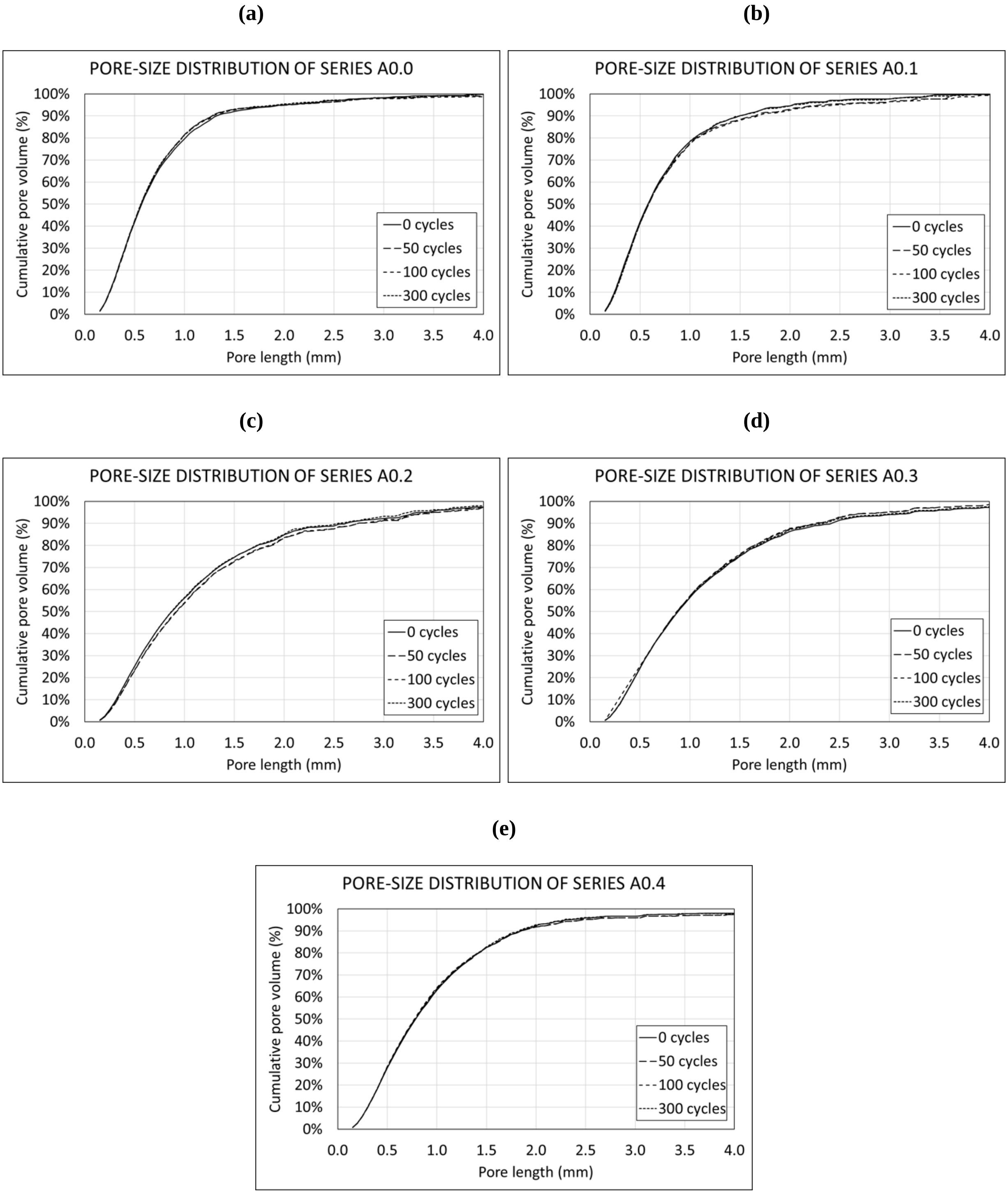

Figure 5. Cumulative pore-volume curves of series A0.0 (a), A0.1 (b), A0.2 (c), A0.3 (d) and A0.4 (e).

Consequently, the results reveal that the increase of the porosity is because the AEA not only generates more pores, but also larger ones.

It is noticed that negligible quantities of AEA do not produce a significant increase in porosity. This could be because of the size of the pores generated not being big enough to be detected by the CT-scan; in this case, under 100 μm. However, as the quantity of AEA increases, stable pores of increasing size are created. Therefore, there is necessarily a percentage limit of AEA for which the size of the pores generated is above the minimum that can be detected by the CT-scan. This fact has two clear consequences. On the one hand, with very low contents of AEA, the porosity measured is almost identical to that belonging to a specimen without AEA. On the other hand, with slightly higher contents, the volume of air initially trapped into non-detectable pores is now considered, hence causing a sudden rise in porosity. In this case, the percentage limit of AEA is placed between 0.1% and 0.2%, which explains the dramatic increase in porosity between series A0.1 and A0.2 (Table 3). Finally, when the amount of AEA is too large, the size of the pores increases and therefore the upward force on them also does. This way, the pore retention capacity inside the concrete matrix decreases, the air is released and hence the porosity decreases. This explains what happens in series A0.4. These results agree with those found by other researchers (Abd Elrahman et al., 2020; Mendes et al., 2017).

On the other side, Figure 4 reveals that freeze-thaw action has a much smaller influence on pore structure than the amount of AEA. However, it is worth highlighting some phenomena that are repeated in all series. Firstly, it is observed that the initial 50 cycles are those showing the greatest impact on concrete microstructure, causing a decrease in porosity. This aspect is more noticeable in the series with more quantity of AEA; in particular, in series A0.4 the reduction in porosity reaches 0.1%. Consequently, a densification of the concrete matrix occurs, which could mean an improvement of its mechanical response. Secondly, over the remaining 250 cycles a gradual recovery of porosity is observed. Again, this increase is greater in the series with higher amount of AEA; in fact, series A0.3 is the only one whose final porosity (after 300 freeze-thaw cycles) overcomes the initial one (with 0 cycles).

When comparing the curves of 300 cycles of all the series, it is observed that, in most of the series, the curve for 300 cycles is below the curves for 0 cycles. On the contrary, in series A0.3, the curve for 300 cycles is above the curve for 0 cycles. However, this variation is small, which means that, in this case, the impact of the freeze-thaw cycles on the concrete matrix is not relevant. This agrees with the visual observation of the specimens at the end of the freeze-thaw cycles process; they did not show apparent signs of damage.

Moreover, Figure 5 reveals that the freeze-thaw action has a very low influence on pore size variations, since cumulative pore-volume curves remain almost unchanged.

These changes in porosity due to freeze-thaw cycles can be explained by the action of two opposite mechanisms. First, a hydration of the cement particles that had not reacted occurs. In the case of high-strength concrete, water/cement ratios often used are very low and a fraction of cement particles remain non-hydrated and, simultaneously, small water bubbles are retained. In addition, the freeze-thaw test conditions, with the specimens completely submerged in water, facilitate the access of water inside concrete. Therefore, local cement hydration reactions are expected to occur, bringing with them an rise in volume of solids and a decrease in porosity. Secondly, the freeze-thaw action results in internal damage inside concrete matrix. This is because during freezing hydraulic pressure on pore-matrix interface significantly increases. If concrete does not have enough tensile strength to withstand this internal pressure, microcracks appear. Consequently, an increase in the total empty space inside the specimens (equivalent to porosity) occurs.

During the first 50 freeze-thaw cycles, a predominance of the hydration mechanism over the microcracking is observed, and hence a global decrease in porosity is produced. Thereafter, non-hydrated cement particles are residual, while the damage caused by freeze-thaw progressively increases. However, this second mechanism is not clearly observed in series A0.0 and A0.1, where the amount of AEA is lower.

3.2. Histogram of pore length

On the basis of the values of length of each individual pore, the histograms of pore length can be plotted. They are graphs that correlate a particular range of pore lengths with the percentage that represents over the total number of pores. These histograms are shown in Figure 6, where it is also included the evolution due to freeze-thaw action. As explained in Section 2, the pores whose length is lower than 0.1 mm have been discarded, since they cannot be defined with enough accuracy or even, they may correspond to digital noise because of the scanning process itself.

Figure 6 reveals that the percentage of pores in all series decreases as the length increases, following a clear negative exponential trend. In fact, pores whose length is between 0.1 and 0.2 mm represent more than 50% of the total pores in all cases.

In addition, other aspects can be outlined in this figure. Firstly, the influence of AEA content is much lower than in porosity curves. However, it seems that its effect continues to be greater than the one belonging to freeze-thaw cycles. If only the 0-cycle bars are taken into account in order to discard the effect of thermal fatigue, it is noticed that the percentage of the smallest pores (0.1-0.2 mm) decreases with the increase in AEA. As a result, the percentage of the remaining pore sizes (0.2-0.6 mm) increases. This is explained by the fact that, as the amount of AEA increases, the pore size also does. Nevertheless, this trend is not repeated in series A0.4, the one containing the largest amount of AEA. As explained above, the reason behind is that, under very high contents of AEA, the pore retention capacity decreases, releasing the entrained air and reducing the porosity.

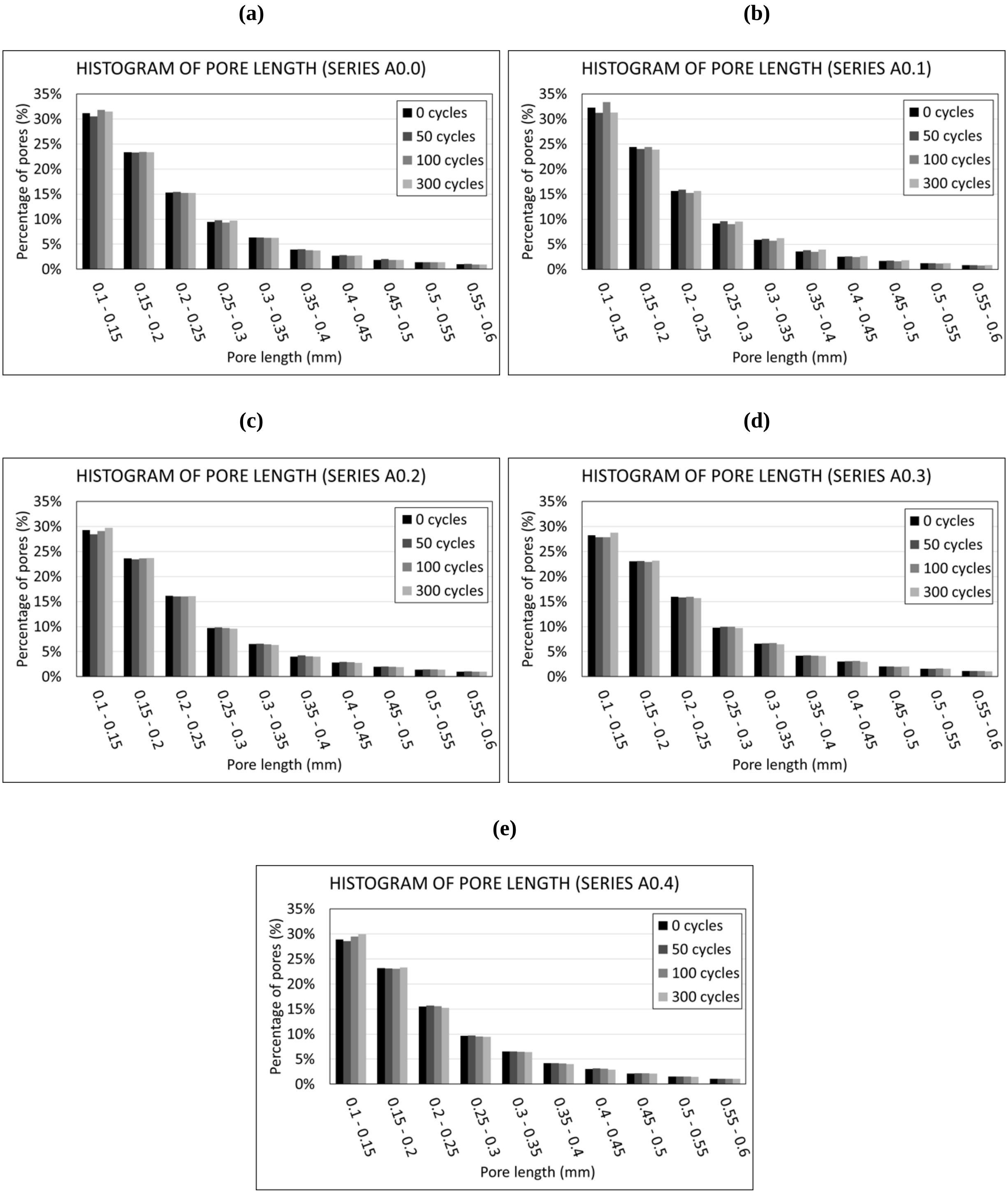

Figure 6. Histogram of pore length of series A0.1 (a), A0.1 (b), A0.2 (c), A0.3 (d) and A0.4 (e).

Secondly, it is noticed that the effect of the freeze-thaw cycles is less significant. A clear tendency is not observed in series A0.0 and A0.1. On the contrary, it seems that in the rest of series the initial 50 cycles reduce the percentage of the smallest pores (0.1-0.2 mm). However, during the rest of cycles a recovery of those pores occurs; in fact, the final percentage of small pores is even higher than the initial one. The aforementioned mechanisms can be used to explain this behavior. During the initial freeze-thaw cycles, local cement hydration reactions predominate. As a result, concrete expansion takes place, which is more likely to affect the smallest pores, closing them and falling in number. Likewise, the internal damage caused by the freeze-thaw cycles predominates over the rest of time. This damage results in microcollapses which disaggregate the pore-matrix interface and, with regard to the CT-scan, this can be read as the division in smaller pores, or even the defects created can be under the detection threshold of the device.

3.3. Histogram of shape factor

One interesting geometrical parameter to characterize pore structure can be obtained from the data provided by both the CT-scan and the DIP software. This is the shape factor, defined as the ratio between the volume of a pore and the volume of the sphere circumscribed to that pore (Eq. (3)) (Blott and Pye, 2008):

$$SF = \frac{V_p}{\frac{1}{6} \cdot \pi \cdot L_p^3} \tag{3}$$

where V_p is the pore volume and L_p is the pore length.

Histograms of shape factor can be plotted by using the data of the shape factor of each individual pore. They consist on graphs that correlate a particular range of shape factors with the percentage that represents over the total number of pores. These histograms are shown in Figure 7, where it is also included the evolution due to freeze-thaw cycles. It should be highlighted that shape factors ranging from 0.8 to 1 are not included, since they represent a very small proportion and do not add any relevant information.

A first conclusion drawn from the histograms in Figure 7 is that pores are not spherical at all, since their shape factors are far from 1. In particular, the modal value varies between 0.2 and 0.4, so the shape of the pores is rather elongated or irregular. This matches with the findings of other recent investigations (Chandrappa and Biligiri, 2018; Vicente et al., 2019a).

Secondly, an increase in shape factor with the amount of AEA is observed; in other words, as the content of AEA increases, pores become more spherical. Moreover, the histograms are flattened simultaneously, which implies a reduction in peak percentages. This suggests that, though the shape factor of the pores increases, it does not tend to stabilize around a certain value. This growth can be explained due to the fact that AEA is able to introduce stable pores inside concrete, whose shape factors are relatively high. This way, the irregularity of pores in the no-AEA situation (series A0.0) is compensated, resulting in higher shape factors. Finally, the trend is reversed in series A0.4 and the shape factor of pores decreases. As explained before, under very high contents of AEA, the pores retention capacity decreases and hence they are released. Therefore, as precisely these microbubbles have a high shape factor, the final result is that pore sphericity is reduced.

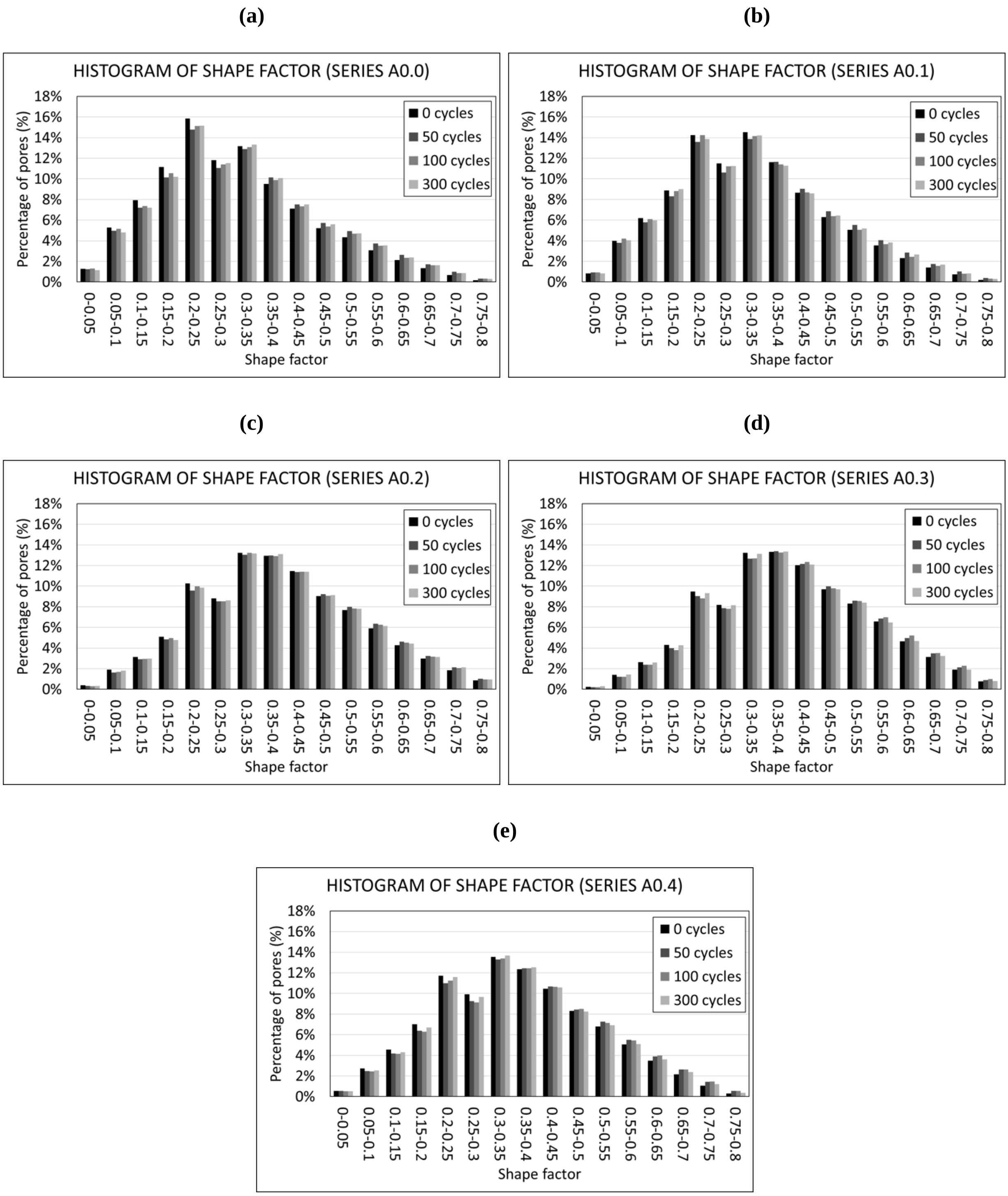

Figure 7. Histogram of shape factor of series A0.0 (a), A0.1 (b), A0.2 (c), A0.3 (d) and A0.4 (e).

Lastly, it is observed that freeze-thaw action barely modifies the shape factor of pores. However, as mentioned above, it seems that the initial 50 cycles have a determining influence. During this period, an increase in shape factor in all series occurs, which is particularly significant in the series with the least content of AEA (series A0.0 and A0.1). This is reflected in a slightly displacement of the histograms to the right. Then, over the rest of the cycles a progressive decrease in shape factor is noticed, and finally the resulting shape factors are very similar to the initial ones. Again, this behavior can be explained due to both the hydration and freeze-thaw damage mechanisms. During the first cycles, local cement hydration reactions cause a concrete expansion that mainly affects the smallest pores, closing them. These pores tend to be precisely more elongated or irregular, thus an increase in shape factor occurs. In the case of the series with larger amounts of AEA, as the pores introduced cause by themselves an increase in shape factor, the effect of hydration mechanism is less relevant. Therefore, the increase in shape factor is lower. Finally, over the rest of cycles, freeze-thaw action causes microcollapses in pores that modify them, making them more irregular or even subdividing them in smaller pores also of irregular shape. In consequence, shape factor decreases.

4. Correlation between internal microstructure and response under freeze-thaw cycles

When the series of 0 cycles and of 300 cycles are compared globally, some trends are observed that can help to understand the relationship between microstructure and macroscopic response.

In the series A0.0 and A0.1 it is observed that the porosity curves at 50, 100 and 300 cycles (Figure 4) are very close to each other, which means that during the first freeze-thaw cycles a densification occurs but, finally, the freeze-thaw cycles do not result in a global damage of the microstructure.

These series have some particular characteristics. First, the porosity in all of them is lower than in the rest of the series. In addition, they initially have a percentage of pores between 0.1 and 0.15 mm higher than the rest. In addition, the maximum pore size is clearly lower. The series A0.0 and A0.1 also show a distribution curve of the shape factor different from the rest of the series. In these cases, the most common range is 0.20-0.25, while for the rest of the series the most common range is clearly higher.

In summary, it is observed that the A0.0 and A0.1 series show the best behavior under freeze-thaw cycles, which are characterized by having less porosity, smaller pores (which are specified in a higher percentage of smaller pores and a smaller maximum pore size) and more elongated pores (with a smaller shape factor).

Apparently, the first freeze-thaw cycles cause a microcracking of the structure, helping to hydrate the cement particles that had not yet been hydrated and ultimately resulting in a reduction in porosity. This process consumes the free water that was inside the specimen. As concrete has low porosity and the pores are small, the entry of water from the outside is very small, that it, they are almost waterproof, so there is less internal damage caused by freeze-thaw cycles.

The series A0.2, A0.3 and A0.4 show a worse behavior under freeze-thaw cycles. By having more porosity, the entry of water from the outside is greater (they are permeable), so the damage caused by freeze-thaw cycles is greater. In addition, they show a higher percentage of larger pores, and also pores with less elongated shapes (larger shape factor). This results in higher values of tensile stresses in the concrete matrix around the pores, caused by the expansion of water when it frozen. It seems that the pores created by the AEA, which tend to be more spherical as explained above, are more vulnerable to the freeze-thaw cycles.

5. Conclusions

In this work, the changes produced in the pore structure of high-strength concrete as a result of the amount of AEA and freeze-thaw cycles are analyzed. For this reason, specimens with five different amounts of AEA have been casted, and then they have been subjected up to 300 freeze-thaw cycles. The specimens have been also scanned using a computed tomography scan at some pre-defined numbers of cycles. The most interesting results are next summarized.

The amount of AEA has a determining influence on porosity. As its content increases, porosity also does, but up to a limit. In this case, that limit is reached in series A0.3, which corresponds to the maximum dosage recommended by the manufacturer. In addition, it is proved that the increase in porosity is due to the fact that AEA is able to generate a greater number of pores and also larger pores. Regarding the reduction in porosity with large amounts of AEA, it is explained because the pore retention capacity inside the concrete matrix decreases.

Freeze-thaw action has less influence on porosity than the amount of AEA. Nevertheless, several interesting phenomena are observed. It is noticed that the initial 50 cycles are those showing the most relevant impact on pore structure, causing a decrease in porosity. However, over the rest 250 cycles a partial recovery of porosity occurs. The final result is that porosity after 300 freeze-thaw cycles is slightly lower in all cases, except for series A0.3, where it remains almost equal. This finding suggests that, under this type of concrete and these test conditions, freeze-thaw action does not substantially damage concrete microstructure. This is clearer in the case of series A0.0 and A0.1, with a lower content of AEA. In these series, the recovery of the porosity after the initial 50 cycles is hardly observed.

The histograms of pore length show that the percentage of pores decreases with increasing length in all series, following a clear negative exponential tendency. On the other side, it seems that the percentage of the smallest pores (0.1-0.2 mm) decreases as the amount of AEA increases, while the rest of pore sizes (0.2-0.6 mm) increases. The reason is that AEA makes larger pores. With regard to the effect of freeze-thaw cycles, it is observed that the first 50 cycles reduce the percentage of the smallest pores (0.1-0.2 mm), which is later recovered over the remaining cycles. Behind this behavior, two opposite mechanisms could be found: concrete hydration and freeze-thaw internal damage.

From the histograms of shape coefficient, it is concluded that pores are not spherical at all, but rather elongated or irregular. In addition, an increase in shape factor with the amount of AEA is observed, which can be explained because the pores generated by AEA are very stable, with a relatively high shape factor. Finally, it is noticed again that the initial 50 freeze-thaw cycles are those which have the greatest influence on pore structure, causing an increase in shape factor.

To sum up, the addition of AEA in concrete mixtures not only affects porosity, but also has a significant impact on pore structure, causing an increase in the number of pores, their size and their shape factor. Alternatively, it seems that freeze-thaw action causes an initial reduction in porosity, which afterwards is gradually recovered. This recover is hardly observed in A0.0 and A0.1 series, with the lowest AEA content, while it is clearly observed in the rest of the series.

In the end, the overall result is that porosity after 300 freeze-thaw cycles decreases slightly in almost all series. Thus, suggesting that freeze-thaw cycles do not damage significantly the microstructure of concrete.

The best response under freeze-thaw cycles is provided by the A0.0 and A0.1 series, since the final porosity is clearly smaller than the initial one. A lower porosity, smaller pores and more elongated pores characterize these series. The first freeze-thaw cycles produce microcracking, which allows the hydration of cement particles that have not been hydrated yet and, consequently, reduce porosity. During the rest of the freeze-thaw cycles, the entry of water from the outside is (modest, limited) ~~small~~, since concrete has low porosity and the pores are small. Concrete is rather waterproof and, in consequence, the internal damage caused by freeze-thaw cycles is exiguous.

6. Acknowledgments

The authors are grateful for the financial support from the Ministerio de Economía y Competitividad, PID2019-110928RB-C32, Spain.

References

Abd Elrahman, M., El Madawy, M.E., Chung, S.-Y., Majer, S., Youssf, O., Sikora, P., 2020. An Investigation of the Mechanical and Physical Characteristics of Cement Paste Incorporating Different Air Entraining Agents using X-ray Micro-Computed Tomography. Crystals 10, 23. https://doi.org/10.3390/cryst10010023

ASTM C226-19, Standard Specification for Air-Entraining Additions for Use in the Manufacture of Air-Entraining Hydraulic Cement, ASTM International, USA, 2019. https://doi.org/10.1520/C0226-19

ASTM C666/C666M-15, Standard Test Method for Resistance of Concrete to Rapid Freezing and Thawing, ASTM International, USA, 2015. https://doi.org/10.1520/C0666_C0666M-15

Balshin, M.Y., 1949. Relation of mechanical properties of powder metals and their porosity and the ultimate properties of porous metal-ceramic materials. Dokl Akad Nauk SSSR 67(5).

Blott, S.J., Pye, K., 2008. Particle shape: a review and new methods of characterization and classification. Sedimentology 55, 31–63. https://doi.org/10.1111/j.1365-3091.2007.00892.x

Chandrappa, A.K., Biligiri, K.P., 2018. Pore structure characterization of pervious concrete using X-ray microcomputed tomography. J. Mater. Civ. Eng. 30, 1–11. https://doi.org/10.1061/(ASCE)MT.1943-5533.0002285

Chen, Y., Wang, K., Wang, X., Zhou, W., 2013. Strength, fracture and fatigue of pervious concrete. Constr. Build. Mater. 42, 97–104. https://doi.org/10.1016/j.conbuildmat.2013.01.006

Dong, Y., Su, C., Qiao, P., Sun, L., 2018. Microstructural damage evolution and its effect on fracture behavior of concrete subjected to freeze-thaw cycles. Int. J. Damage Mech. 27, 1272–1288. https://doi.org/10.1177/1056789518787025

Fan, Z., Sun, Y., 2019. Detecting and evaluation of fatigue damage in concrete with industrial computed tomography technology. Constr. Build. Mater. 223, 794–805. https://doi.org/10.1016/j.conbuildmat.2019.07.016

Gao, J., Sha, A., Wang, Z., Hu, L., Yun, D., Liu, Z., Huang, Y., 2018. Characterization of carbon fiber distribution in cement-based composites by Computed Tomography. Constr. Build. Mater. 177, 134–147. https://doi.org/10.1016/j.conbuildmat.2018.05.114

González, D.C., Mínguez, J., Vicente, M.A., Cambronero, F., Aragón, G., 2018. Study of the effect of the fibers' orientation on the post-cracking behavior of steel fiber reinforced concrete from wedge-splitting tests and computed tomography scanning. Constr. Build. Mater. 192, 110–122. https://doi.org/10.1016/j.conbuildmat.2018.10.104

Gu, C., Sun, W., Guo, L., Wang, Q., Liu, J., Yang, Y., Shi, T., 2018. Investigation of Microstructural Damage in Ultrahigh-Performance Concrete under Freezing-Thawing Action. Adv. Mater. Sci. Eng. 2018, 1–9. https://doi.org/10.1155/2018/3701682

Han, N., Tian, W., 2018. Experimental study on the dynamic mechanical properties of concrete under freeze-thaw cycles. Struct. Concr. 19, 1353–1362. https://doi.org/10.1002/suco.201700170

Hasselman, D.P.H., 1963. Relation Between Effects of Porosity on Strength and on Young's Modulus of Elasticity of Polycrystalline Materials. J. Am. Ceram. Soc. 46, 564–565. https://doi.org/10.1111/j.1151-2916.1963.tb14615.x

Jasiūnienė, E., Cicėnas, V., Grigaliūnas, P., Rudžionis, Ž., Navickas, A.A., 2018. Influence of the rheological properties on the steel fibre distribution and orientation in self-compacting concrete. Mater. Struct. Constr. 51. https://doi.org/10.1617/s11527-018-1231-y

Jianxun, C., Xizhong, Z., Yanbin, L., Xianghui, D., Qin, L., 2014. Investigating freeze-proof durability of C25 shotcrete. Constr. Build. Mater. 61, 33–40. https://doi.org/10.1016/j.conbuildmat.2014.02.077

Kim, H.K., Jeon, J.H., Lee, H.K., 2012. Workability, and mechanical, acoustic and thermal properties of lightweight aggregate concrete with a high volume of entrained air. Constr. Build. Mater. 29, 193–200. https://doi.org/10.1016/j.conbuildmat.2011.08.067

Kosior-Kazberuk, M., 2013. Variations in fracture energy of concrete subjected to cyclic freezing and thawing. Arch. Civ. Mech. Eng. 13, 254–259. https://doi.org/10.1016/j.acme.2013.01.002

Le, H.T., Kraus, M., Siewert, K., Ludwig, H.-M., 2015. Effect of macro-mesoporous rice husk ash on rheological properties of mortar formulated from self-compacting high performance concrete. Constr. Build. Mater. 80, 225–235. https://doi.org/10.1016/j.conbuildmat.2015.01.079

Luo, Q., Liu, D., Qiao, P., Feng, Q., Sun, L., 2017. Microstructural damage characterization of concrete under freeze-thaw action. Int. J. Damage Mech. 27, 1–18. https://doi.org/10.1177/1056789517736573

Ma, Z., Zhao, T., Yang, J., 2017. Fracture Behavior of Concrete Exposed to the Freeze-Thaw Environment. J. Mater. Civ. Eng. 29, 04017071. https://doi.org/10.1061/(ASCE)MT.1943-5533.0001901

Mendes, J.C., Moro, T.K., Figueiredo, A.S., Silva, K.D. do C., Silva, G.C., Silva, G.J.B., Peixoto, R.A.F., 2017. Mechanical, rheological and morphological analysis of cement-based composites with a new LAS-based air entraining agent. Constr. Build. Mater. 145, 648–661. https://doi.org/10.1016/j.conbuildmat.2017.04.024

Mínguez, J., Vicente, M.A., González, D.C., 2019. Pore morphology variation under ambient curing of plain and fiber-reinforced high performance mortar at an early age. Constr. Build. Mater. 198, 718–731. https://doi.org/10.1016/j.conbuildmat.2018.12.010

Netinger Grubeša, I., Marković, B., Vračević, M., Tunkiewicz, M., Szenti, I., Kukovecz, Á., 2019. Pore Structure as a Response to the Freeze/Thaw Resistance of Mortars. Materials (Basel). 12, 3196. https://doi.org/10.3390/ma12193196

Nitka, M., Tejchman, J., 2018. A three-dimensional meso-scale approach to concrete fracture based on combined DEM with X-ray μCT images. Cem. Concr. Res. 107, 11–29. https://doi.org/10.1016/j.cemconres.2018.02.006

Oesch, T., Landis, E., Kuchma, D., 2018. A methodology for quantifying the impact of casting procedure on anisotropy in fiber-reinforced concrete using X-ray CT. Mater. Struct. Constr. 51.

https://doi.org/10.1617/s11527-018-1198-8

Olawuyi, B.J., Boshoff, W.P., 2017. Influence of SAP content and curing age on air void distribution of high performance concrete using 3D volume analysis. Constr. Build. Mater. 135, 580–589. https://doi.org/10.1016/j.conbuildmat.2016.12.128

Rouquerol, J., Avnir, D., Fairbridge, C.W., Everett, D.H., Haynes, J.H., Pernicone, N., Ramsay, J.D.F., Sing, K.S.W., Unger, K.K., 1994. Recommendations for the characterization of porous solids (Technical Report), Pure and Applied Chemistry. https://doi.org/10.1351/pac199466081739

Ryshkewitch, E., 1953. Compression Strength of Porous Sintered Alumina and Zirconia. J. Am. Ceram. Soc. 36, 65–68. https://doi.org/10.1111/j.1151-2916.1953.tb12837.x

Schiller, K.K., 1958. Porosity and strength of brittle solids (with particular reference to gypsum), in: Mechanical Properties of Non-Metallic Brittle Materials. pp. 35–49.

Shen, A., Lin, S., Guo, Y., He, T., Lyu, Z., 2018. Relationship between flexural strength and pore structure of pavement concrete under fatigue loads and Freeze-thaw interaction in seasonal frozen regions. Constr. Build. Mater. 174, 684–692. https://doi.org/10.1016/j.conbuildmat.2018.04.165

Shields, Y., Garboczi, E., Weiss, J., Farnam, Y., 2018. Freeze-thaw crack determination in cementitious materials using 3D X-ray computed tomography and acoustic emission. Cem. Concr. Compos. 89, 120–129. https://doi.org/10.1016/j.cemconcomp.2018.03.004

Skarżyński, Ł., Marzec, I., Tejchman, J., 2019. Fracture evolution in concrete compressive fatigue experiments based on X-ray micro-CT images. Int. J. Fatigue 122, 256–272. https://doi.org/10.1016/j.ijfatigue.2019.02.002

Skarżyński, Ł., Suchorzewski, J., 2018. Mechanical and fracture properties of concrete reinforced with recycled and industrial steel fibers using Digital Image Correlation technique and X-ray micro computed tomography. Constr. Build. Mater. 183, 283–299. https://doi.org/10.1016/j.conbuildmat.2018.06.182

Suzuki, T., Shiotani, T., Ohtsu, M., 2017. Evaluation of cracking damage in freeze-thawed concrete using acoustic emission and X-ray CT image. Constr. Build. Mater. 136, 619–626. https://doi.org/10.1016/j.conbuildmat.2016.09.013

Tian, W., Han, N., 2018. Pore characteristics (>0.1 mm) of non-air entrained concrete destroyed by freeze-thaw cycles based on CT scanning and 3D printing. Cold Reg. Sci. Technol. 151, 314–322. https://doi.org/10.1016/j.coldregions.2018.03.027

UNE-EN 12390-3. Ensayos de hormigón endurecido. Parte 3: Determinación de la resistencia a compresión de probetas, AENOR, Spain, 2020.

UNE-EN 206. Hormigón. Especificaciones, prestaciones, producción y conformidad, AENOR, Spain, 2018.

Vicente, Miguel A, González, D.C., Mínguez, J., 2019. Recent advances in the use of computed tomography in concrete technology and other engineering fields. Micron 118, 22–34. https://doi.org/10.1016/j.micron.2018.12.003

Vicente, M.A., González, D.C., Mínguez, J., 2014. Determination of dominant fibre orientations in fibre-reinforced high-strength concrete elements based on computed tomography scans. Nondestruct. Test. Eval. 29, 164–182. https://doi.org/10.1080/10589759.2014.914204

Vicente, M.A., González, D.C., Mínguez, J., Tarifa, M.A., Ruiz, G., Hindi, R., 2018a. Influence of the pore morphology of high strength concrete on its fatigue life. Int. J. Fatigue 112, 106–116. https://doi.org/10.1016/j.ijfatigue.2018.03.006

Vicente, Miguel A., Mínguez, J., González, D.C., 2019a. Variation of the pore morphology during the early age in plain and fiber-reinforced high-performance concrete under moisture-saturated curing. Materials (Basel). 12. https://doi.org/10.3390/ma12060975

Vicente, M.A., Mínguez, J., González, D.C., 2017. The Use of Computed Tomography to Explore the Microstructure of Materials in Civil Engineering: From Rocks to Concrete, in: Mesrur-Halefoğlu, A. (Ed.), Computed Tomography. Advanced Applications. IntechOpen, pp. 207–229. https://doi.org/10.5772/intechopen.69245

Vicente, Miguel A., Ruiz, G., González, D.C., Mínguez, J., Tarifa, M., Zhang, X., 2019b. Effects of fiber orientation and content on the static and fatigue behavior of SFRC by using CT-Scan technology. Int. J. Fatigue 128, 105178. https://doi.org/10.1016/j.ijfatigue.2019.06.038

Vicente, M.A., Ruiz, G., González, D.C., Mínguez, J., Tarifa, M., Zhang, X., 2018b. CT-Scan study of crack patterns of fiber-reinforced concrete loaded monotonically and under low-cycle fatigue. Int. J. Fatigue 114, 138–147. https://doi.org/10.1016/j.ijfatigue.2018.05.011

Vydra, V., Vodák, F., Kapičková, O., Hošková, Š., 2001. Effect of temperature on porosity of concrete for nuclear-safety structures. Cem. Concr. Res. 31, 1023–1026. https://doi.org/10.1016/S0008-8846(01)00516-6

Yang, X., Shen, A., Guo, Y., Zhou, S., He, T., 2018. Deterioration mechanism of interface transition zone of concrete pavement under fatigue load and freeze-thaw coupling in cold climatic areas. Constr. Build. Mater. 160, 588–597. https://doi.org/10.1016/j.conbuildmat.2017.11.031

Zhao, Y., Wang, X., Jiang, J., Zhou, L., 2019. Characterization of interconnectivity, size distribution and uniformity of air voids in porous asphalt concrete using X-ray CT scanning images. Constr. Build. Mater. 213, 182–193. https://doi.org/10.1016/j.conbuildmat.2019.04.056

Zhou, H., Li, H., Abdelhady, A., Liang, X., Wang, H., Yang, B., 2019. Experimental investigation on the effect of pore characteristics on clogging risk of pervious concrete based on CT scanning. Constr. Build. Mater. 212, 130–139. https://doi.org/10.1016/j.conbuildmat.2019.03.310

AUTHORSHIP STATEMENT

MANUSCRIPT TITLE:

Influence of air-entraining agent and freeze-thaw action on pore structure in high-strength concrete by using CT-Scan technology.

AUTHORS:

Dorys C. González (DCG), Álvaro Mena (AM), Jesús Mínguez, (JM), Miguel A. Vicente (MAV)

All persons who meet authorship criteria are listed as authors, and all authors certify that they have participated sufficiently in the work to take public responsibility for the content, including participation in the concept, design, analysis, writing, or revision of the manuscript.

Furthermore, each author certifies that this material or similar material has not been and will not be submitted to or published in any other publication before its appearance in the journal "Cold Regions Science and Technology".

Category 1

Conception and design of study: DCG, AM, JM, MAV.

Acquisition of data: AMA, JM

Analysis and/or interpretation of data: DCG, MAV.

Category 2

Drafting the manuscript: AM, JM, DCG

Revising the manuscript critically for important intellectual content: DCG, MAV

Category 3

Approval of the version of the manuscript to be published (the names of all authors must be listed): DCG, AM, JM, MAV.